ARTICLE

Monolayer behaviour in bulk ReS$_2$ due to electronic and vibrational decoupling

Sefaattin Tongay[1,2], Hasan Sahin[3], Changhyun Ko[2], Alex Luce[2], Wen Fan[2,4], Kai Liu[2], Jian Zhou[1,2], Ying-Sheng Huang[5], Ching-Hwa Ho[5], Jinyuan Yan[6], D. Frank Ogletree[7], Shaul Aloni[7], Jie Ji[4], Shushen Li[1], Jingbo Li[1], F.M. Peeters[3] & Junqiao Wu[1,2,8]

Semiconducting transition metal dichalcogenides consist of monolayers held together by weak forces where the layers are electronically and vibrationally coupled. Isolated monolayers show changes in electronic structure and lattice vibration energies, including a transition from indirect to direct bandgap. Here we present a new member of the family, rhenium disulphide (ReS$_2$), where such variation is absent and bulk behaves as electronically and vibrationally decoupled monolayers stacked together. From bulk to monolayers, ReS$_2$ remains direct bandgap and its Raman spectrum shows no dependence on the number of layers. Interlayer decoupling is further demonstrated by the insensitivity of the optical absorption and Raman spectrum to interlayer distance modulated by hydrostatic pressure. Theoretical calculations attribute the decoupling to Peierls distortion of the 1T structure of ReS$_2$, which prevents ordered stacking and minimizes the interlayer overlap of wavefunctions. Such vanishing interlayer coupling enables probing of two-dimensional-like systems without the need for monolayers.

[1] State Key Laboratory of Superlattices and Microstructures, Institute of Semiconductors, Chinese Academy of Sciences, P.O. Box 912, Beijing 100083, People's Republic of China. [2] Department of Materials Science and Engineering, University of California, Berkeley, California 94720, USA. [3] Department of Physics, University of Antwerp, Groenenborgerlaan 171, Antwerpen B-2020, Belgium. [4] Department of Thermal Science and Energy Engineering, University of Science and Technology of China, Anhui 230027, China. [5] Department of Electronic Engineering, National Taiwan University of Science and Technology, Taipei 106, Taiwan. [6] Advanced Light Source, Lawrence Berkeley National Laboratory, Berkeley, California 94720, USA. [7] Molecular Foundry, Lawrence Berkeley National Laboratory, Berkeley, California 94720, USA. [8] Materials Sciences Division, Lawrence Berkeley National Laboratory, Berkeley, California 94720, USA. Correspondence and requests for materials should be addressed to J.W. (email: wuj@berkeley.edu).

Atomically thin monolayer transition metal dichalcogen-ides (sTMDs) are a new class of two-dimensional (2D) materials with the chemical formula MX_2, where M is a transition metal (Mo, W and Re) and X is a chalcogen (S, Se and Te) element. Monolayer sTMDs are promising functional materials for next-generation flexible optoelectronics and photo-voltaics applications owing to their mechanical flexibility, chemically and environmentally stability, optical properties and low operating voltages in various device configurations[1–3]. One of the landmark features of sTMDs is that they undergo a crossover from indirect bandgap in the bulk to direct bandgap in monolayers[4], and as a result, monolayer sTMDs become direct-gap semiconductors that absorb and emit light efficiently. Currently, this crossover has been observed in all members of the sTMDs family known in the field, and is attributed to a strong interlayer coupling and explained as a confinement effect in the thickness direction.

Here we present a new member of the sTMDs family, rhenium disulphide (ReS_2), in which the band renormalization is absent and the bulk behaves as electronically and vibrationally decoupled monolayers. Such unique response originates from lack of interlayer registry and weak interlayer coupling arising from Peierls distortion of the 1T structure of ReS_2, as confirmed by high-resolution transmission electron microscopy (HRTEM), electron diffraction and density functional theory (DFT) calculations. Consequently, from bulk to monolayers, ReS_2 remains a direct-bandgap semiconductor, its photoluminescence (PL) intensity increases, whereas its Raman spectrum remains unchanged with increasing number of layers. Even after further modulating the interlayer distance (coupling) by external hydrostatic pressure, the optical absorption and Raman spectrum remain unchanged, implying that the interlayer interaction is indeed rather weak. The presented results establish ReS_2 as an unusual, new member of the sTMDs family where the bulk acts as if it is electronically and vibrationally monolayers.

Results

DFT calculations and calculated crystal structure. Figure 1a shows a comparison of the structure of a single layer of ReS_2 with the conventional 1H structure of sTMDs such as MoS_2. For ReS_2,

DFT calculations show that the hexagonal (H) phase is unstable, whereas the octahedral (T) phase goes through the Peierls distortion, resulting in buckled S layers and zigzag Re chains along one of the lattice vectors in the plane (Fig. 1a bottom, Supplementary Fig. 1). The resultant lattice in Fig. 1a can be regarded as a distorted 1T structure (Supplementary Notes 1 and 2). Owing to the reduced crystal symmetry, ReS_2 displays a more complex Raman spectrum than conventional sTMDs, as will be discussed later. DFT calculations reveal that bulk and monolayer ReS_2 have nearly identical band structures (Fig. 1b), both being direct-bandgap semiconductors with a predicted generalized gra-dient approximation (GGA) bandgap at $E_{gap} = 1.35$ eV (bulk) and 1.43 eV (monolayer), respectively (Supplementary Note 3). This is in stark contrast to conventional sTMDs, where the band structure is strongly dependent on the number of layers[4,5]. Our DFT calculations (Fig. 1c) also show that adjacent layers in ReS_2 are indeed only weakly coupled to each other, with a coupling energy of ∼18 meV per unit cell, <8% of that of MoS_2 (460 meV for the corresponding 2×2 conventional cell).

HRTEM measurements and determination of crystal structure. To study the structure and define the stacking order of ReS_2, we deployed extensive HRTEM and electron diffractometry measurements. In Fig. 2a, we display the HRTEM image taken from two ReS_2 flakes, one with the layers perpendicular (red square) and the other parallel (green square) to the electron beam, confirming high crystallinity of the exfoliated ReS_2. This arrangement is convenient as it provides a view of the crystalline structure from two orthogonal directions. Fast Fourier transform images taken perpendicular to the planes displays quasi-hexagonal pattern formed by (100), (001) and (110) reflections with the diffraction spot width defined by the beam convergence (∼0.1 mrad) (Fig. 2b top), consistent with a well-defined crystalline structure (simulated kinematic diffraction patterns in Fig. 2c top). To provide insight into the layer stacking order, we have oriented the crystal with the electron beam pointing at the [210] axis. The diffraction pattern consists of $(1\bar{2}0)$ and (002) reflections (Fig. 2b,c bottom). The lack of odd ((001), (003), (005) and so on.) reflections suggests lack of specific (Bernal) stacking,
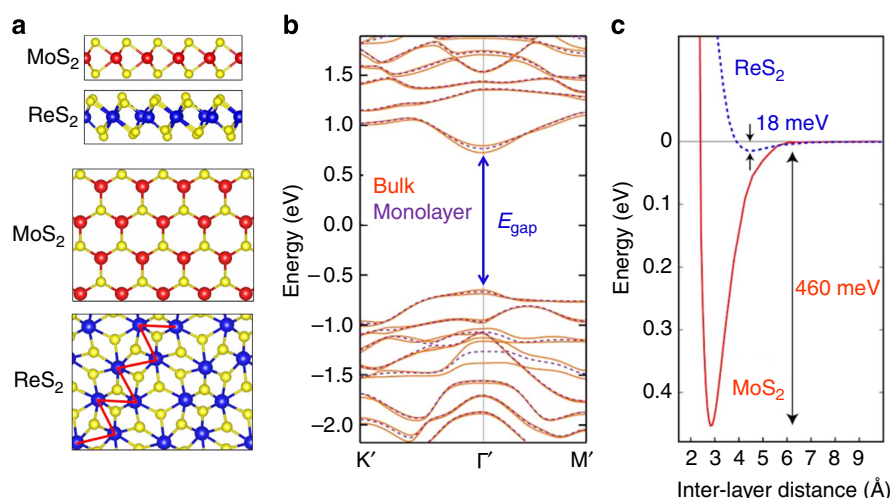
Figure 1 | Different crystal structure and band structure of ReS₂ from conventional sTMDs. (**a**) Side (top two panels) and top view (bottom two panels) of ReS_2 with distorted 1T crystal structure compared with the 1H structure of conventional sTMDs. The Re atoms dimerize as a result of the Peierls distortion forming a Re chain denoted by the red zigzag line. (**b**) DFT calculated electronic band structure of bulk (orange solid curves) and monolayer (purple dashed curves) ReS_2. Both are predicted to be a direct bandgap semiconductor with nearly identical bandgap value at the Γ point. (**c**) The calculated total energy of the system as a function of interlayer separation. The significantly shallower depth of the well in ReS_2 implies much weaker interlayer coupling energy in ReS_2 as compared with MoS_2.
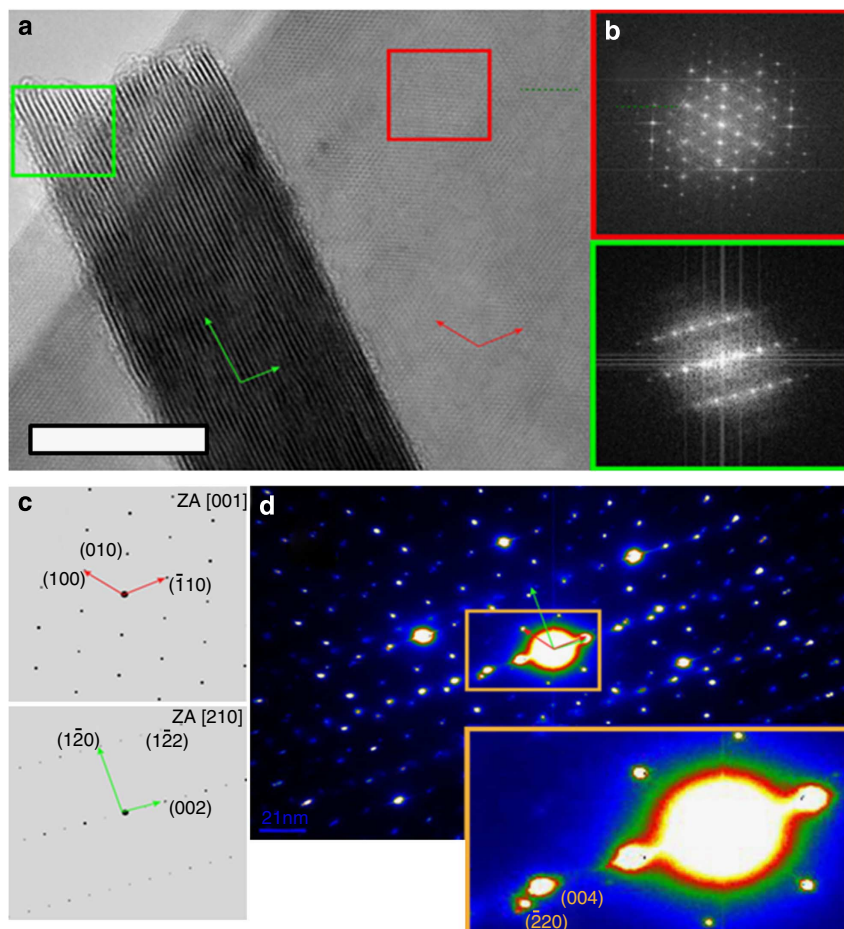
Figure 2 | Structural characterization of ReS$_2$. (**a**) HRTEM images taken from ReS$_2$ along in- and out-of-plane directions. There are two flakes: one flake's basal plane is perpendicular to the electron beam (red square box) and the other flake's basal plane is oriented parallel to the beam (green square box). Scale bar, 20 nm. (**b**) Fast Fourier transform images from the denoted red/green windows. (**c**) Simulated kinematic diffraction patterns, and (**d**) nano-beam electron diffraction pattern. Inset: Zoom-in image to the nano-beam electron diffraction pattern.

unlike in 2H-MoS$_2$ that possesses Bernal stacking between the layers. The $(0,0,2l)$ reflections are inhomogeneously broadened both in the 001 and $(1\bar{2}0)$ directions. Nano-beam electron diffraction pattern in Fig. 2d and inset allow direct comparison of the broadening because of the particular sample geometry. For simplicity, we attribute all the inhomogeneous broadening of the $0,0,2l$ reflections to fluctuation in interlayer distance. From this analysis, the interlayer spacing is determined to vary between 6.0 and 6.9 Å. This reduced degree of crystallinity is not turbostratic in nature; rather, it is a consequence of weak interlayer bonding with small in-plane displacements from equilibrium position (Supplementary Notes 1,2 and 7).

Comparison between PL behaviour of ReS$_2$ versus other sTMDs. Considering such contrast in the crystal structure, we next focus experimentally on the physical properties of ReS$_2$ flakes. Mono- and multilayer ReS$_2$ were mechanically exfoliated from synthetic bulk crystals (see Methods section for crystal growth) onto Si substrates with 90 nm thermal oxide[6]. These ReS$_2$ flakes were characterized using atomic force microscopy (AFM), Raman spectroscopy, micro-PL (µPL), and nano-Auger electron spectroscopy (AES). Nano-AES elemental composition analysis revealed an S/Re ratio of 1.98 ± 0.10 (Supplementary Fig. 8, Supplementary Note 6). Tapping-mode AFM scan typically yielded 0.7 nm thickness for the monolayers. For comparison, monolayers and multilayers of conventional sTMDs (MoS$_2$,

MoSe$_2$, WSe$_2$ and WS$_2$) were also prepared by mechanical exfoliation from bulk crystals.

All ReS$_2$ flakes exhibit µPL at room temperature with a peak in the range of 1.5–1.6 eV. The peak energy increases slightly (by <10%) for an isolated monolayer (Fig. 3a). The integrated PL intensity increases with the number of layers, and starts to saturate for flakes thicker than six layers, as shown in Fig. 3b. This is in stark contrast to the behaviour observed in conventional sTMDs such as MoS$_2$ (ref. 4), MoSe$_2$ (ref. 7), WS$_2$ and WSe$_2$ (ref. 8), where the monolayer PL intensity is enhanced by orders of magnitude as a result of the crossover from an indirect bandgap in the bulk to a direct bandgap in monolayers. In those Mo and W systems, the PL in the indirect-bandgap multilayers arises from hot luminescence[4] across the wider direct bandgap, and is exponentially weaker in thicker layers. In addition, the PL peak position of these conventional sTMDs increases drastically by 30–60% for thinner layers (Fig. 3c), which can be explained by stronger out-of-plane quantum confinement with decreasing thickness[4]. In contrast, the PL peak of ReS$_2$ is nearly independent of the number of layers, indicating that thinning down the flake does not enhance the quantum confinement of electrons in the system, and that neighbouring monolayers in the flake are already largely electronically decoupled.

Electronic decoupling in ReS$_2$. To further test the interlayer decoupling in ReS$_2$, we modulate its interlayer distance by
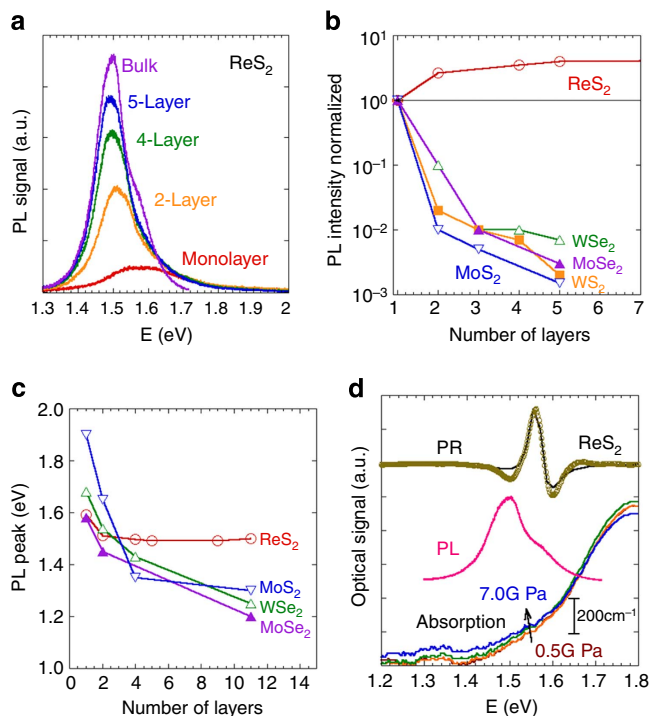
Figure 3 | Optical properties of ReS₂ in comparison with conventional sTMDs. (**a**) PL spectrum of ReS₂ flakes with different number of layers. (**b**) Integrated PL intensity as a function of number of layers (normalized to that of monolayer) in ReS₂, MoS₂, MoSe₂, WS₂ and WSe₂. (**c**) Change in the PL peak position as a function of number of layers in ReS₂, MoS₂, MoSe₂ and WSe₂. (**d**) Absorption coefficient of a bulk ReS₂ flake (thickness ~10 μm) at hydrostatic pressures ranging from 0.5 to 7.0 GPa. Also shown is the PL and photo-modulated reflectance spectra of bulk ReS₂ taken at ambient condition. It can be seen that a direct bandgap exists at 1.55 ± 0.05 eV and is insensitive to the pressure.

applying hydrostatic pressure using a diamond anvil cell (DAC). The hydrostatic pressure is applied via a liquid medium onto a bulk flake (~10 μm), where the pressure is calibrated with the standard Ruby luminescence[9] (Supplementary Note 5). The transparent DAC window allows experiments for micro-Raman and optical micro-absorption. Comparing the absorption curves with the PL and photo-modulated reflectance (see Supplementary Fig. 7, Supplementary Note 5) spectra in Fig. 3d, the bandgap of ReS₂ is determined to be $E_{gap} = 1.55$ eV, close to the DFT calculated E_{gap}. In Fig. 3d, the optical absorption curve shows nearly no change under the application of hydrostatic pressure up to 7 GPa. The out-of-plane linear elastic moduli of ReS₂ and MoS₂ are estimated to be 0.4 and 20 GPa, respectively, calculated from the second derivative of the interlayer coupling energy in Fig. 1c. Therefore, a pressure of 7 GPa would significantly reduce their interlayer distance. In bulk MoS₂ where adjacent layers are coupled, the pressure dependence of the bandgap is $dE_{gap}/dP \sim 0.02$ eV per GPa (refs 10,11), corresponding to a 0.14-eV shift of the absorption edge for the pressure range in Fig. 3d, whereas ReS₂ shows a total shift of 0.04 eV at the most. Therefore, the overlap of electron wavefunctions from adjacent layers is much weaker in ReS₂ than in MoS₂, such that a modulation of the interlayer distance cannot renormalize the band structure in the former.

Vibrational decoupling in ReS₂. The much weaker interlayer interaction energy shown in Fig. 1c also leads to a decoupling of

lattice vibrations between adjacent layers in ReS₂. In Fig. 4a,b, we compare calculated phonon dispersion with the measured Raman spectrum of monolayer ReS₂. The Raman spectrum displays at least 11 modes in the 100–400 cm⁻¹ range, which is significantly more than for sTMDs with higher crystal symmetries. These Raman peaks are mostly caused by the low crystal symmetry and are associated with fundamental Raman modes (A₁g, E₂g, and E₁g) coupled to each other and to acoustic phonons. The two most prominent Raman peaks are at 163 and 213 cm⁻¹, respectively, and correspond to the in-plane (E₂g) and mostly out-of-plane (A₁g-like) vibration modes (Supplementary Fig. 6, Supplementary Note 3). Comparison between the Raman spectra of monolayer and bulk ReS₂ (Fig. 4c) does not show detectable changes within the 0.3 cm⁻¹ resolution. Again in contrast, the Raman spectrum is known to be highly sensitive to the number of layers in MoS₂ (Fig. 4d) and other sTMDs[12–14]. For example, going from the bulk to monolayer sTMDs, the E₂g mode in MoS₂ typically stiffens by ~5 cm⁻¹, and the A₁g mode typically softens by a similar amount. As ReS₂ is vibrationally decoupled, its Raman spectrum is expected to be also less sensitive to hydrostatic pressure compared with other sTMDs. In Fig. 5a, we present the pressure induced change in the most prominent Raman peaks for bulk ReS₂ and MoS₂. As the interlayer coupling directly affects the out-of-plane vibration modes, we focus on the pressure behaviour of the Raman peaks associated with the out-of-plane vibration. The primarily out-of-plane, Ag-like Raman peak in ReS₂ located at 213 cm⁻¹ stiffens by only ~1 cm⁻¹ per GPa of hydrostatic pressure, whereas it is >2.7 cm⁻¹ per GPa for the Ag mode in MoS₂, 2.2 cm⁻¹ per GPa in MoSe₂ and 2.5 cm⁻¹ per GPa in MoTe₂ (ref. 15). In Fig. 5b, these numbers are compared against each other. Because the 213 cm⁻¹ vibration mode in ReS₂ is not purely Ag, but mixed with the more pressure-sensitive, in-plane Eg mode (see Supplementary Note 3), the intrinsic pressure coefficient of the Ag mode is expected to be even lower in ReS₂. Moreover, considering the ~50 times lower elastic modulus of ReS₂ than MoS₂, the deformation coefficient (dAg/dz, where z is interlayer distance) of out-of-plane vibration in ReS₂ is estimated to be orders of magnitude lower than MoS₂. Related to the observed electronic and vibrational decoupling in ReS₂, the out-of-plane thermal conductivity is also calculated and found to be much smaller than that of MoS₂ ($\kappa^{\perp}_{MoS_2}/\kappa^{\perp}_{ReS_2} \approx 42$), whereas the in-plane thermal conductivity of ReS₂ and MoS₂ are on the same order of magnitude (Supplementary Note 4).

Discussion

On the basis of the distorted crystal structure, we discuss the physical origin of the vanishing interlayer coupling in ReS₂. We first note that each Re atom has seven valence electrons and therefore has one extra electron in the 1T or H structure. DFT calculations show that when this electron contributes to the formation of Re–Re bonds, the total energy of the system is lowered, the Eigen values of the acoustic phonons become real and the lattice becomes a distorted 1T structure as shown in Fig. 1a (Supplementary Notes 1 and 2). Upon transition from 1T (1H) to the distorted 1T structure, the energy gain is 1.1 (0.9) eV per ReS₂ molecule. In the distorted 1T structure, the Re atoms in the layer dimerize in such a way that they form a zigzag Re–Re chain extending along one of the lattice vectors[16,17]. Interestingly, by geometry consideration, the presence of the Re chains eliminates the energy benefit for the ReS₂ layers to order in Bernal (AB) or rhombohedral (ABC) stacking that occurs in other sTMDs. Our DFT calculations show that while sliding one MoS₂ monolayer over the other, one yields variation in total energy of ~200 meV; for ReS₂ the energy difference is just on the order of 5 meV (Supplementary Note 2). The lack of ordered stacking
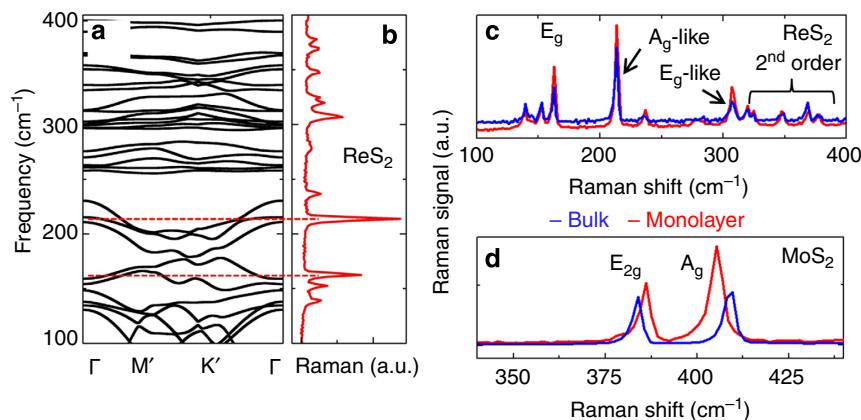
Figure 4 | Vibrational properties of ReS$_2$ and Raman spectra. (a) Calculated phonon dispersion for monolayer ReS$_2$. The phonon dispersion of bulk ReS$_2$ (Supplementary Fig. 6) remains nearly identical to that of monolayer. **(b)** Raman spectrum measured on a monolayer ReS$_2$. **(c)** Raman spectrum taken on bulk (blue) and monolayer (red) ReS$_2$. **(d)** Same on MoS$_2$. The Raman spectrum of ReS$_2$ shows no thickness dependence, whereas the MoS$_2$ in-plane (E$_{2g}$) and out-of-plane (A$_{1g}$) peaks are highly sensitive to the number of layers.
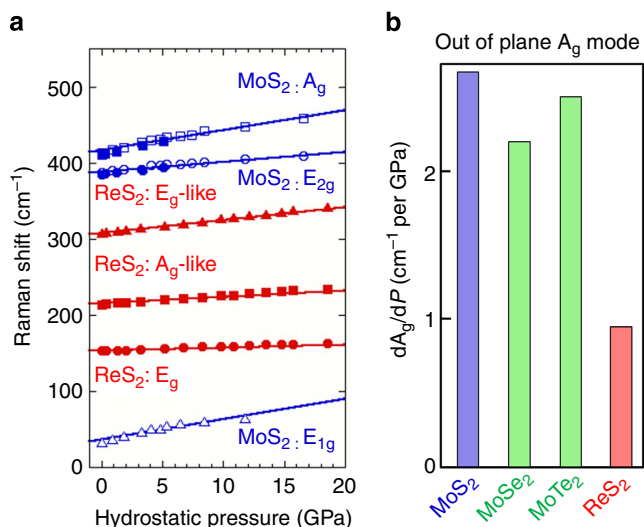
Figure 5 | Pressure dependence of Raman peaks of ReS$_2$ compared with MoS$_2$. (a) Variation of the most prominent Raman peaks of bulk ReS$_2$ and MoS$_2$ as a function of applied hydrostatic pressure. Empty blue points are taken from ref. 15, and filled red and blue points are from this work. The pressure dependence of MoS$_2$ A$_g$ and E$_{2g}$ peaks is confirmed by the good agreement between this work and ref. 15. The straight lines are linear fit to the experimental data. **(b)** Comparison of pressure coefficient (dA$_g$/dP) of the out-of-plane (A$_g$) Raman peaks of MoS$_2$, MoSe$_2$, MoTe$_2$ and ReS$_2$. It can be seen that the ReS$_2$ out-of-plane vibration shows at least a factor of 2 weaker dependence on pressure.

significantly reduces the interlayer coupling energy, akin to turbostratic graphite where the interlayer interaction is significantly weaker than that of Bernal-stacked graphite. Another factor contributing to the vanishing interlayer coupling comes from a much weaker polarization inside the ReS$_2$ layers. Our charge density calculations show that, compared with MoS$_2$, there is a smaller charge difference between the neighbouring Re and S planes, and hence a smaller dipole moment residing in each layer. As a result of the weak intra-layer polarization, the van der Waals force and the binding energy between adjacent ReS$_2$ layers are very weak (Supplementary Fig. 4).

Therefore, ReS$_2$ bulk crystals would be an ideal platform to probe 2D excitonic and lattice physics, circumventing the

challenge of preparing large-area, single-crystal monolayers. Experiments on 2D systems that are currently limited by the availability of large-area monolayers or by low sensitivity to monolayer thickness would become possible on the bulk ReS$_2$. In this sense, the presented results introduce a new type of sTMDs with distinct physical properties from conventional members of the sTMDs explored to date.

Methods

Micro-Raman and μPL experiments. Raman and PL measurements were performed using a × 100 objective in a Renishaw micro-Raman/PL system. The excitation laser wavelength is 488 nm, with laser power ranging from 100 to 1,000 μW power on a ~6-μm^2 spot.

DAC measurements. Two symmetric DACs with type II diamonds of 300 and 500 μm flat culets were utilized for Raman and optical absorption experiments, respectively. The pressure volume of 120 μm in height and 70 μm in diameter was machined from a 250-μm-thick stainless steel gaskets. A methanol–ethanol mixture of 4:1 volume ratio was used as a pressure transmitting medium. Hydrostatic pressure applied inside the chamber hole was calibrated by measuring the R1 PL line shift of ruby. A series of Raman spectra were taken on a ReS$_2$ single-crystal flake at various pressures up to 26 GPa using a × 50 magnification, 18-mm working distance objective, on the Renishaw micro-Raman/PL system. For optical absorption measurements with the DAC, a home-built optics system equipped with a 0.5-m single-grating monochromator and a tungsten–halogen lamp was used. The sample flake was magnified and imaged on the focal plane, where an apertured silicon photodiode detects the light intensity with a lock-in amplifier.

ReS$_2$ growth. Single crystals of ReS$_2$ were grown by the chemical vapour transport method, using Br$_2$ as a transport agent, leading to n-type conductivity. Before the crystal growth, quartz tubes containing Br$_2$ and the reacting elements (Re: 99.95% pure; S: 99.999%) were evacuated and sealed. The quartz tube was placed in a three-zone furnace and the charge pre-reacted for 24 h at 800 °C with the growth zone at 1,000 °C, thereby preventing transport of the product. The furnace was then equilibrated to give a constant temperature across the reaction tube and was programmed over 24 h to produce the temperature gradient at which single-crystal growth takes place. The best results were obtained with a temperature gradient of 1,060 to 1,100 °C.

High-resolution TEM. HRTEM and diffractometry was performed on JEOL2100F microscope equipped with EDS and EELS spectrometers. The exfoliated ReS$_2$ was transferred to electron transparent supports (C-flat carbon support and patterned SiN membranes from EMS). A number of 20–50-nm-thick ReS$_2$ crystals were studied in various orientations including the in-plane and out-of-plane configurations.

DFT calculations. Structural, electronic and vibrational properties have been calculated using GGA-PBE (Perdew-Burke-Ernzerhof) functional, as implemented in the VASP code[18,19] within the DFT, which is demonstrated to yield rather

accurate results for sTMDs. Calculations were performed using the Generalized Gradient Approximation[20] and projector augmented-wave potentials[21]. The kinetic energy cutoff for the plane-wave basis set was 500 eV. In the self-consistent potential and total energy calculations of ReS$_2$ layers, a set of $(31 \times 31 \times 1)$ k-point samplings was used for Brillouin zone integration. The convergence criterion of self-consistent calculations for ionic relaxations was 10^{-5} eV between two consecutive steps. By using the conjugate gradient method, all atomic positions and unit cells were optimized until the atomic forces were <0.01 eV/Å. Pressures on the lattice unit cell were decreased to values <0.5 kbar. Phonon dispersion curves were obtained using the small displacement method[22].

References

1. Wang, Q. H., Kalantar-Zadeh, K., Kis, A., Coleman, J. N. & Strano, M. S. Electronics and optoelectronics of two-dimensional transition metal dichalcogenides. *Nat. Nanotech.* **7,** 699–712 (2012).
2. Radisavljevic, B., Radenovic, A., Brivio, J., Giacometti, V. & Kis, A. Single-layer MoS$_2$ transistors. *Nat. Nanotech.* **6,** 147–150 (2012).
3. Chhowalla, M. *et al.* The chemistry of two-dimensional layered transition metal dichalcogenide nanosheets. *Nat. Chem.* **5,** 263–275 (2013).
4. Mak, K., Lee, C., Hone, J., Shan, J. & Heinz, T. F. Atomically thin MoS$_2$: a new direct-gap semiconductor. *Phys. Rev. Lett.* **105,** 136805 (2010).
5. Splendiani, A. *et al.* Emerging photoluminescence in monolayer MoS$_2$. *Nano Lett.* **10,** 1271–1275 (2010).
6. Novoselov, K. S. *et al.* Two-dimensional atomic crystals. *Proc. Natl Acad. Sci. USA* **102,** 10451–10453 (2005).
7. Tongay, S. *et al.* Thermally driven crossover from indirect toward direct bandgap in 2D semiconductors: MoSe$_2$ versus MoS$_2$. *Nano Lett.* **12,** 5576–5580 (2012).
8. Zhao, W. *et al.* Evolution of electronic structure in atomically thin sheets of WS$_2$ and WSe$_2$. *ACS Nano* **7,** 791–797 (2013).
9. Mao, H. K., Xu, J. & Bell, P. M. Calibration of the ruby pressure gauge to 800 kbar under quasi-hydrostatic conditions. *J. Geophys. Res.: Solid Earth* **91,** 4673–4676 (1986).
10. Webb, A. W., Feldman, J. L., Skelton, E. F. & Towle, L. C. High pressure investigations of MoS$_2$. *J. Phys. Chem. Solids* **37,** 329–335 (1976).
11. Connell, G. A. N., Wilson, J. A. & Yoffe, A. D. Effects of pressure and temperature on exciton absorption and band structure of layer crystals: Molybdenum disulphide. *J. Phys. Chem. Solids* **30,** 287–296 (1969).
12. Lee, C. *et al.* Anomalous lattice vibrations of single- and few-layer MoS$_2$. *ACS Nano* **4,** 2695–2700 (2010).
13. Sahin, H. *et al.* Anomalous Raman spectrum and dimensionality effects in WSe$_2$. *Phys. Rev. B* **87,** 165409 (2013).
14. Berkdemir, A. *et al.* Identification of individual and few layers of WS$_2$ using Raman Spectroscopy. *Sci. Rep.* **3,** 1755 (2013).
15. Sugai, S. & Ueda, T. High-pressure Raman spectroscopy in the layered materials 2H-MoS$_2$, 2H-MoSe$_2$, and 2H-MoTe$_2$. *Phys. Rev. B* **26,** 6554–6558 (1982).
16. Ho, C. H., Huang, Y. S., Tiong, K. K. & Liao, P. C. Absorption-edge anisotropy in ReS$_2$ and ReSe$_2$ layered semiconductors. *Phys. Rev. B* **58,** 16130–16135 (1998).
17. Friemelt, K. *et al.* Scanning tunneling microscopy with atomic resolution on ReS$_2$ single crystals grown by vapor phase transport. *Ann. Phys.* **1,** 248–253 (1992).
18. Kresse, G. & Hafner, J. Ab initio molecular dynamics for liquid metals. *Phys. Rev. B* **47,** 558–561 (1993).
19. Kresse, G. & Furthmuller, J. Efficient iterative schemes for ab initio total-energy calculations using a plane-wave basis set. *Phys. Rev. B* **54,** 11169–11186 (1996).
20. Perdew, J. P., Burke, K. & Ernzerhof, M. Generalized gradient approximation made simple. *Phys. Rev. Lett.* **77,** 3865–3868 (1996).
21. Grimme, S. Semiempirical GGA-type density functional constructed with a long-range dispersion correction. *J. Comput. Chem.* **27,** 1787–1799 (2006).
22. Alfe, D. PHON A program to calculate phonons using the small displacement method. *Comp. Phys. Commun.* **180,** 2622–2633 (2009).

Author contributions

S.T. and J.W. conceived and designed the measurements. S.T. performed all optical experiments. C.K. and D.F.O. contributed to nano-AES experiments. C.K., J.Y. and A.L. performed DAC measurements. W.F., J.J., J.Z., Y.-S.H., C.-H.H. and K.L. prepared crystals and flakes for AFM, scanning electron microscopy, TEM and optical measurements. S.A. performed HRTEM experiments and provided interpretation. H.S., S.L., J.L. and F.M.P. carried out theoretical analysis and DFT calculations. All authors read and edited the manuscript.

Additional information

Supplementary Information accompanies this paper at http://www.nature.com/nature communications.

Competing financial interests: The authors declare no competing financial interests.

Reprints and permission information is available online at http://npg.nature.com/reprintsandpermissions/

How to cite this article: Tongay, S. *et al.* Monolayer behaviour in bulk ReS$_2$ due to electronic and vibrational decoupling. *Nat. Commun.* 5:3252 doi: 10.1038/ncomms4252 (2014).
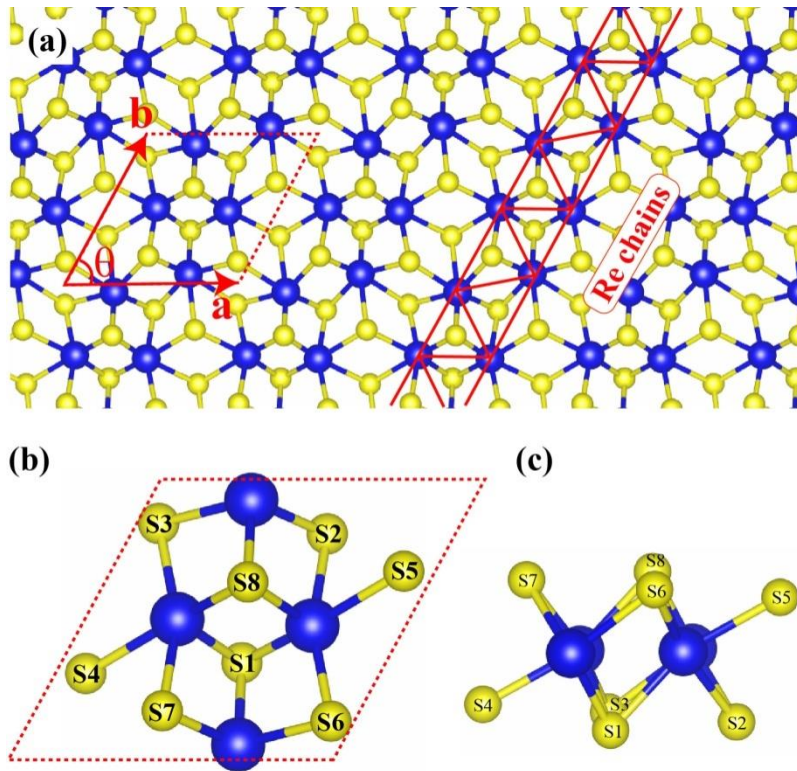
Supplementary Figure 1. (a) Top view of atomic structure of a monolayer ReS_2. Unit cell and Re chains are indicated. (b) Top and (c) Side view of the ReS_2 monolayer is shown by unit cell atoms.
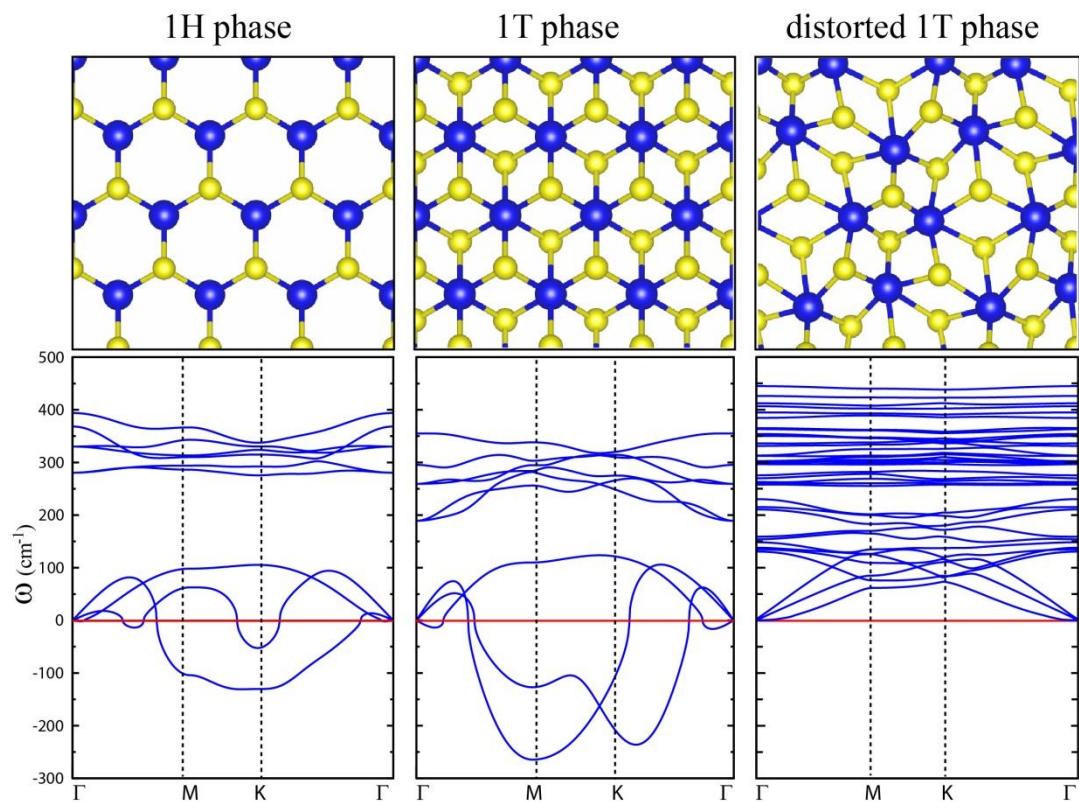
Supplementary Figure 2. Phonon dispersions of unstable 2×2 supercell of 1H and 1T phases of ReS$_2$. Also shown in the ground-state stable structure, distorted 1T.
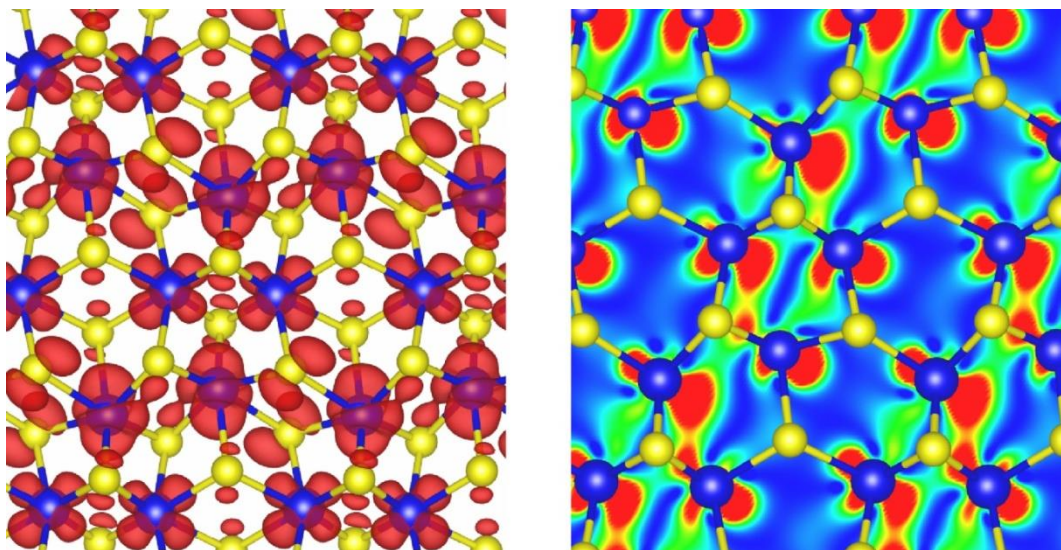
Supplementary Figure 3. (a) Calculated 3D and b. 2D charge density of anti-bonding (left) and bonding states (right) of a monolayer ReS$_2$. States at the $\mathbf{\Gamma}$-point are shown.
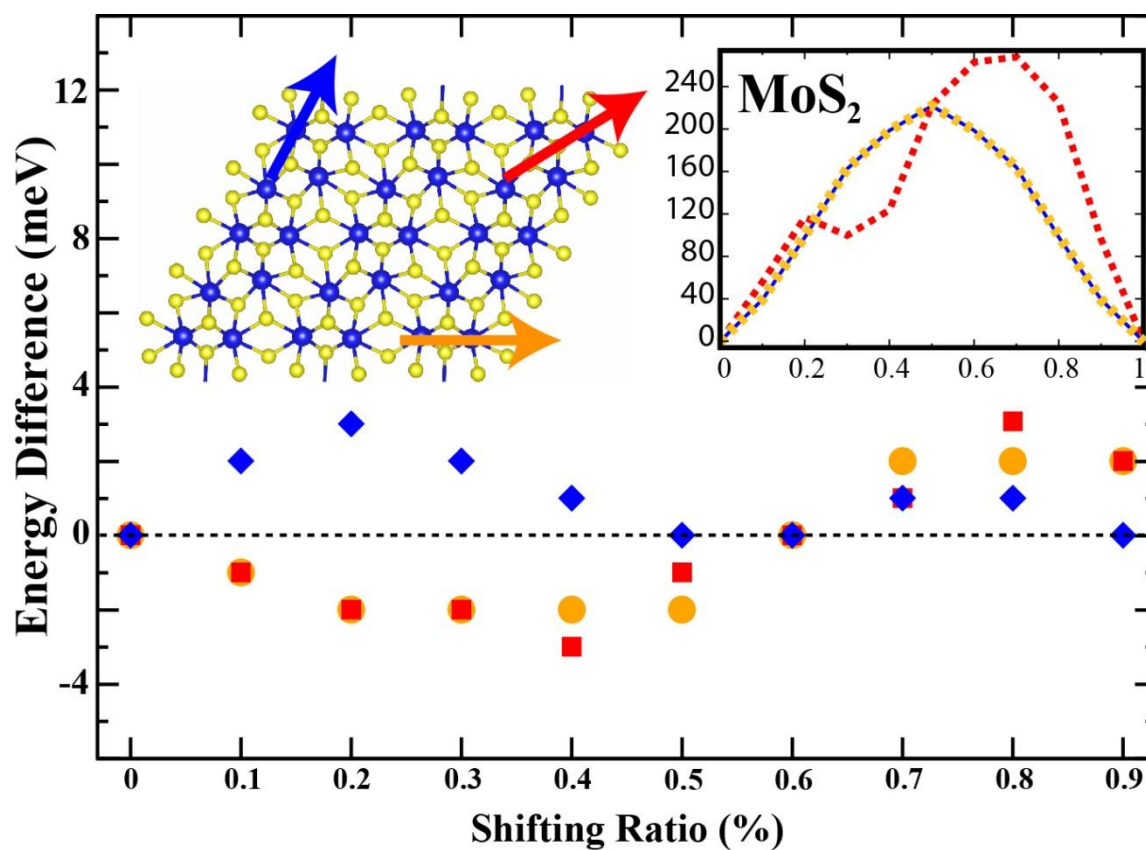
Supplementary Figure 4. Comparison of interlayer interaction energy of ReS_2 as a function of in-plane translation along three different directions. The shifting ratio is the displacement divided by the lattice constant along that direction. Inset: same calculations for MoS_2 layers.
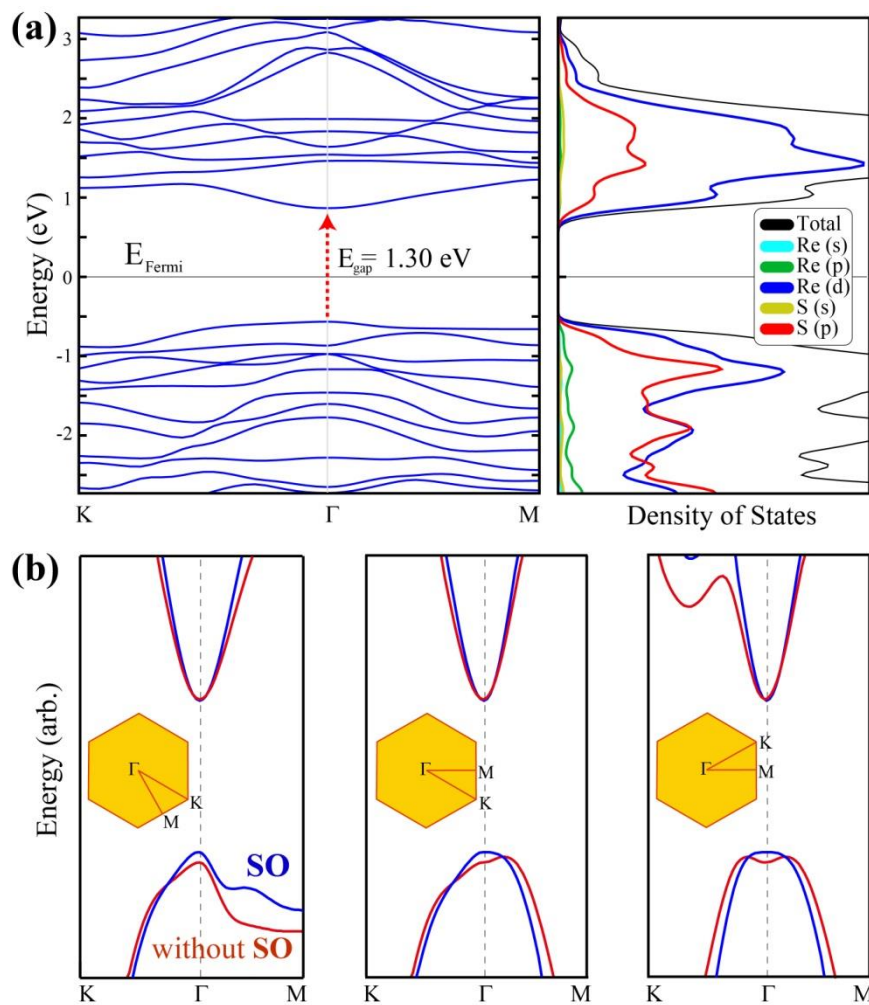
Supplementary Figure 5. (a) Electronic band dispersion (GGA+SO) and partial density of states of monolayer ReS_2. (b) Due to the broken symmetry, band edges have slightly different characters at different K (and M) points of the hexagonal Brillouin zone. All the band edges show semiconducting behaviour with direct bandgap, while indirect transitions appear only when spin-orbit interactions are ignored.
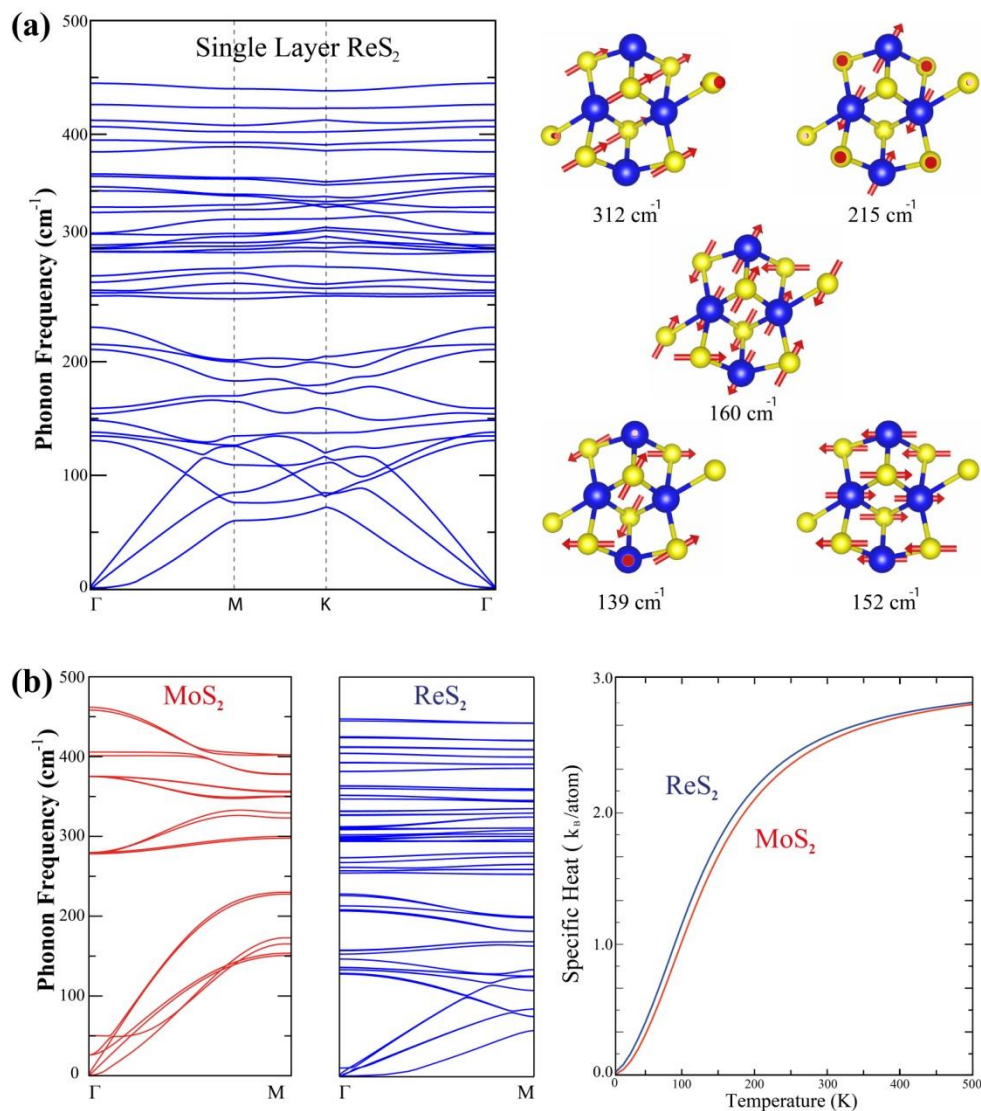
Supplementary Figure 6. (a) Phonon dispersion of monolayer ReS_2. The phonon branches which are Raman-active are shown in the right panel. The 215 cm^{-1} mode is largely out-of-plane, which is experimentally observed as 213 cm^{-1} and analysed in details in the main text. (b) Phonon dispersions and calculated specific heat of bulk MoS_2 and ReS_2.
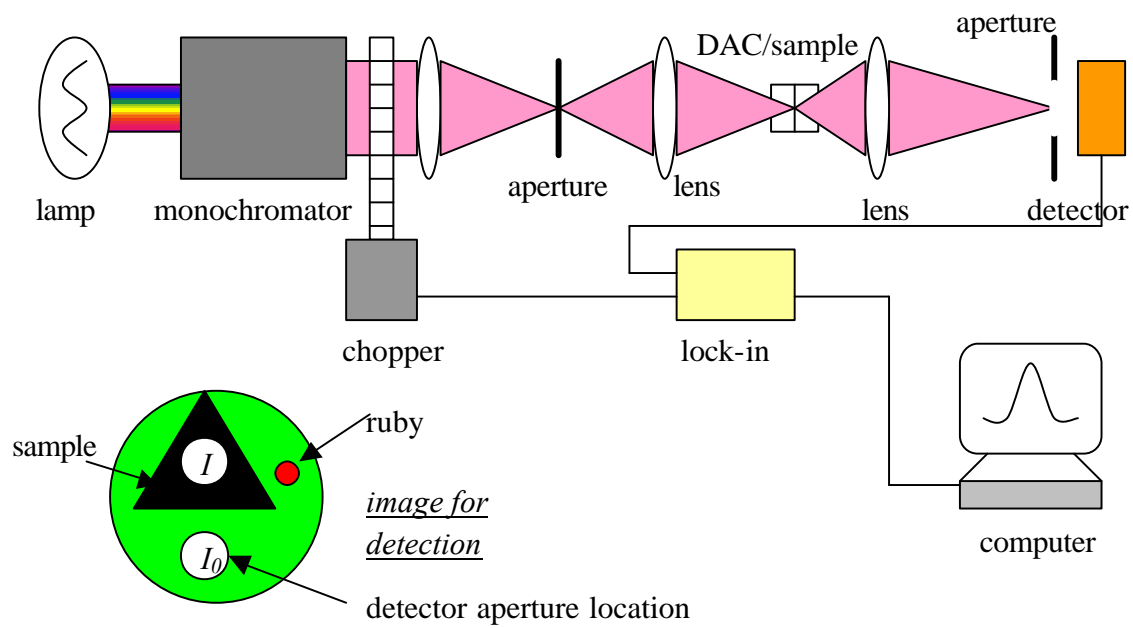
Supplementary Figure 7. Setup to measure optical absorption of bulk ReS$_2$ flakes at different hydrostatic pressures.
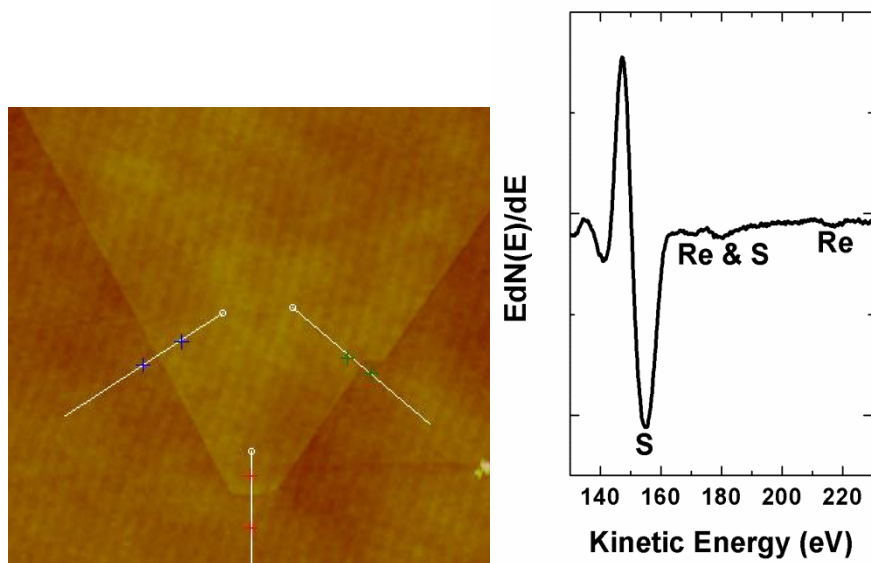
Supplementary Figure 8. (Left) AFM topography of a monolayer ReS_2 exfoliated on SiO_2 surface. The area of scan is 1.5 by 1.5 μm, and the monolayer height is ~ 0.7nm. (Right) Nano-AES spectrum taken on a ReS_2 flake using 3 keV excitation. The S/Re ratio is estimated to be ~ 1.98±0.10.

Supplementary Note 1. Lattice Structure of ReS$_2$. Each ReS$_2$ layer resembles the 1T crystal structure, which is also the ground state of some other transition metal dichalcogenides (TMDs), such as TaS$_2$, TaSe$_2$, TiS$_2$, VSe$_2$ and MnTe$_2$. However, differing from these and other sTMDs such as MoS$_2$, MoSe$_2$ and WSe$_2$, ReS$_2$ crystallizes in a distorted T structure with clustering of Re$_4$ units forming a one-dimensional chain inside each monolayer. The formation of parallel chains of Re$_4$ clusters in ReS$_2$ causes a lattice distortion from the ideal octahedral layered structure. In Fig. S1, we present the optimized atomic structure of ReS$_2$. The monolayer ReS$_2$ can be thought as a distorted 1T structure. Due to metal-metal bonding, the unit cell of ReS$_2$ is doubled and therefore its primitive cell is composed of four Re and eight S atoms. As shown in Fig. S1b, closer view of its atomic structure reveals that the S atoms locate at four different distances from the Re layer. The formation of local Re chains along the b lattice vector breaks the hexagonal lattice symmetry and makes this structure special. In addition to the anisotropy between out-of-plane and in-plane crystal directions, basal plane anisotropy along *a* and *b* lattice vectors can be observed.

Our vibrational analysis shown in Fig. S2, reveals that the periodic 1H and 1T structures of ReS$_2$ can be obtained by total energy optimization calculations. The calculated lattice constants in H and T structures are 6.62 and 6.19 Å, respectively (2×2 super-cells of these correspond to a unit cell of ReS$_2$). The lattice parameters of ReS$_2$ in distorted 1T phase are a = 6.51 and b = 6.41 Å. However, further examination of the stability of these structures shows that the H and T structures of ReS$_2$ are unstable, as their LA and ZA phonon modes have imaginary eigen-frequencies. It is calculated that ReS$_2$ single layer lowers its energy, 1.1 eV (0.9) per ReS$_2$ molecule, for a transition from 1T (1H) to distorted 1T phase. Clearly, both energy optimization and phonon calculations reveal that ReS$_2$ layers have distorted 1T phase in their ground state.

The formation of Re chains can be understood via analysis of the bonding nature of ReS$_2$. As shown in Fig. S3, band decomposed charge density analysis shows that there is significant amount of bond charges between the Re-Re dimers. It appears that each Re atom with seven valence electrons would have one dangling electron in its 1T (and H) structure. Therefore, obviously Re atoms lower the total energy of the system by making covalent bonds with each other. As seen from Fig. S3, the reason for the formation of Re chains are the extra electrons that result in strong covalent bonding between the Re atoms. However, the 5d-3p hybridized bonding states provide interaction between adjacent Re chains. Therefore these Re chains are further bonded to each other via S atoms.

Supplementary Note 2. Inter-layer Stacking of ReS$_2$. We showed that differing from MoS$_2$ bilayers that have 460 meV interlayer binding, ReS$_2$ bilayers are weakly bonded to each other with 18 meV. The interlayer binding of ReS$_2$ layers is found to be small even by LDA calculations that are known to give overestimate for these types of structures. For ReS$_2$ (MoS$_2$), calculated values of inter-layer binding energy per MX$_2$ molecule by using GGA, GGA+vdW and LDA exchange correlation functionals are 2 (58), 30 (76) and 38 (170) meV, respectively. Our calculations also revealed that shifting one ReS$_2$ monolayer over another does not result in any significant change in total energy. With the translation along a, b lattice vectors and along the diagonal direction of the unit cell, the energy difference between the different stacking positions is negligibly small (at most 7 meV). These energies are shown in Fig.S4.Therefore we can conclude that the interlayer interaction is extremely weak for adjacent ReS$_2$ layers and for the bulk (or multilayer) ReS$_2$ structure; *i.e.*, any kind of ordered stacking is experimentally possible. Similar calculation of sliding MoS$_2$ single-layer over the other one (started from the ground state configuration) gives energy differences for different positions in the order of 200 meV and rather large energy differences compared to ReS$_2$.

The reason of the vanishing inter-layer coupling can be understood by analysis of charges on each Re and S layer. Our results reveal that the Re layer becomes positively charged while outermost S layers are negatively charged after the formation of the distorted 1T (1T*) structure of ReS_2. Here the situation is similar to $1H-MoS_2$. However, the charge difference between Mo and S atoms is 1.8 electrons per unit cell, whereas in ReS_2 this difference is just 0.4 electron/unit cell. Since the intra-layer polarization between Re and S layers is much weaker than that between Mo and S layers, van der Waals (vdW) - like interaction is much weaker in ReS_2. Therefore, compared to Mo, the one dangling electron on the Re atom results in less intra-layer polarization and weakens the vdW-like inter-layer interaction.

Supplementary Note 3. Electronic Structure and Lattice Dynamics. Bulk ReS_2 is a diamagnetic semiconductor crystallized in a distorted T structure of triclinic symmetry. Due to its distorted layered lattice structure, anisotropic electrical and optical properties along a, b and c lattice vectors can be expected. In Fig. S5 we present calculated electronic band dispersion and partial density of states (DOS) for monolayer ReS_2. It is seen that ReS_2 has a semiconducting band structure with a direct bandgap at the Γ point. From partial DOS analysis we see that both the valence and conduction band edges are composed of Re-d and S-p states. It is also worth to note that the majority of the states at these band edges originate from Re-d states.

Differing from Figure.1b, in order to see how spin-orbit (SO) interaction influences the band structure of ReS_2, GGA+SO band dispersion is presented. It is seen that while the dispersion of the bands do not change considerably, the bandgap of single layer ReS_2 decreases from 1.43 to 1.30 eV. Since the perfect hexagonal unit cell of 1T structure is disturbed after the formation of Re chains, corners of the Brillouin Zone of the distorted 1T phase shifts negligibly. Moreover, zoomed-in plots for band edges in Fig. S5 reveal the importance of inclusion of spin-orbit interactions in the distorted 1T phase. As long as SO interactions are taken into account, band edges leads to a direct bandgap and therefore for a correct description of band dispersion, inclusion of SO effects is essential.

For determination of the dispersion of phonon branches, we perform first-principles calculations by using 48 and 96 atom unit cells for monolayer and bulk structures, respectively. In Fig. S6 we take a closer look at the lattice dynamics of monolayer ReS_2. As a result of the lattice distortion, the lattice symmetry of ReS_2 is broken and hence it has 36 non-degenerate eigen-modes. In phonon dispersion of bulk ReS_2 which is shown in Fig. S6b number of modes is doubled. Although most of these are mixing of in-plane and out-of-plane motion of Re and S atoms, certain modes have a more characteristic behaviour. The bond-stretching nature of the modes at 152, 160 and 215 cm^{-1} implies the possibility for the observation in Raman measurements. Our calculations displays twenty nine phonon branches (fifty eight for bulk) in the 100 ~ 400 cm^{-1} range and we observe eleven of them as Raman-active. It is also worth to note that because insufficient number of grid-points in the FFT-mesh along the directions of c lattice-vector, lower-most acoustic mode has imaginary eigen-frequency at the Γ point. This imaginary eigenvalue that has no physical meaning is just a numerical artifact. Due to large computational cost of calculating phonons of such 48- and 96-atomic systems with a very fine FFT-mesh, numerical error in lower-most modes was fixed by quadratic fitting.

Supplementary Note 4. **Thermal Conductivity of ReS_2 and MoS_2.** In the main text, we discuss that the weak interlayer coupling in ReS_2 manifests itself as electronic and vibrational decoupling; as a result, bulk ReS_2 behaves as if monolayers. The discussed weak coupling also suggests that out-of-plane thermal conductivity for ReS_2 should be lower compared to other sTMDs (such as MoS_2) where the layers are coupled much stronger.

The thermal conductivity properties were calculated using Debye's model. The lattice thermal conductivity of a structure can be expressed by the $\kappa = (1/3)C_v\upsilon^2\tau$ where C_v, υ and τ are specific heat, phonon velocity and phonon relaxation lifetime, respectively and the effective phonon mean free path (MFP) is $\Lambda = \upsilon\tau$. At high temperatures, almost all the phonon modes become excited and Umklapp scattering becomes the dominant interaction process between phonons. Around the Debye temperature, the most energetic phonon's wavelength approaches size of the unit cell size. In such case, Debye temperature (Θ) relates to the in-plane lattice constant a and group velocity υ by the formal relation $\Theta=(2h\upsilon)/(ak_B)$. Using the experimentally available Debye temperature values ($\Theta_{MoS2}=570$ and $\Theta_{ReS2}=196$ K)[23-24] one can extract the υ parameter.

In Fig.S6, we present volumetric specific heat C_v in units of k_B per atom in the unit cell of bulk ReS$_2$ and MoS$_2$ that are extracted from the calculated phonon dispersion relations. At the same time, MFP ratio of $\Lambda_{MoS2}/\Lambda_{ReS2}$ approaches the ratio of the average inter-atomic distances a_{MoS2}/a_{ReS2} for relatively high temperatures. Using the C_V, Λ, and υ ratios calculated from experimentally available Debye temperature temperatures using the $\Theta=(2h\upsilon)/(ak_B)$ relation, the in-plane thermal conductivity of ReS$_2$ and MoS$_2$ ($\kappa_{MoS2}/\kappa_{ReS2}$) has a ratio of 1.34.

It is generally known that the contribution of out-of-plane lattice vibrations to thermal conductivity is rather small in layered materials such as graphene and sTMDs. The Slack's approach provides a successful model, and has been widely applied to various types of semiconductors.[25] Following Slack's theory, out-of-plane κ can be given by $\kappa = (\mathcal{M}B\delta\Theta_D^3)/(T\gamma_G^2N^{2/3})$, where $\mathcal{M}$ is the average atomic mass, B is a physical constant (3.1×10^{-6}), δ^3 is the average volume occupied by one atom of the crystal, Θ_D is the Debye temperature, γ_G is the Gruneisen parameter, and N is the number of atoms per unit cell. We can calculate the Gruneisen parameter of each mode from the relative shift in the corresponding branch $\gamma_{G,s} = -(V/\omega_s)(\partial\omega_s/\partial V)$. Here ω_s is the angular frequency of phonon of the mode indexed by s, and V is the volume of the considered unit cell. Since the different phonon branches show different dependence on the lattice expansion, one has to take the averaged frequency shift over all the phonon modes that can contribute to cross-plane conductivity. By doing so, the average value of the out-of-plane Gruneisen parameter is calculated to be $\gamma^\perp_{MoS2}= 0.5$ for MoS$_2$. Because of the broken symmetry and the larger unit cell of the distorted-T structure of ReS$_2$, we found ~50 phonon branches that all possibly contribute to the out-of-plane heat conduction. For example, it is found that these modes exhibit 0.9-4.2 cm^{-1} red shift under 0.002 lattice expansion. From these shifts, we calculated $\gamma^\perp_{ReS2}= 0.8$. Combined with all other parameters, this yields $\kappa^\perp_{MoS2}/\kappa^\perp_{ReS2} \approx 42$.

It is also worth noting that for layered materials, the presence of a ZO' mode located just above the acoustic modes is another indication of the strength of layer-layer coupling.[26-27] For instance, graphene's ZO' mode appears at 133 cm^{-1}, while for MoS$_2$ it is at 50 cm^{-1} (See Figure S6(b). However, because of the weak coupling between adjacent layers in ReS$_2$, ZO' mode is at 11 cm^{-1}, implying that the interlayer interaction is rather small compared to other sTMDs (Figure S6(b)).

In conclusion, our results confirm that because of the weak interaction between the adjacent ReS$_2$ layers, out-of-plane thermal conductivity of ReS$_2$ is more than an order magnitude lower than MoS$_2$. Such difference in the out-of-plane thermal conductivity is mostly associated with differences in the Gruneisen parameter and Debye temperature. Furthermore, the presence of corrugations and thermally excited distortions may lead to symmetry breaking in lattice structures and therefore the symmetry selection rules, which determine how phonons are scattered, may differ.

Supplementary Note 5. Micro-Absorption through the Diamond Anvil Cell (DAC) and Photo-Modulated Reflectance. Optical absorption measurements were performed using a 0.5 m single-grating monochromator and a silicon photodiode detector. Figure S7 shows experimental setup [28]. The sample in the tiny pressurized volume of the diamond anvil cell (DAC) is magnified (by ~ 50×) through a short-focus lens. Near the focal plane, a magnified image of the sample and surrounding empty area in the pressurized volume is obtained. A small aperture is inserted into the image plane, through which the light intensity can be selectively detected. When the aperture is placed in the shadow of the sample, the light intensity is scanned and recorded as I; when the aperture is located in the empty area, I_0 is recorded. The absorption coefficient α is then calculated as α(hν) = ln[I_0(hν)]/ln[I(hν)]/thickness. The reflection of the beam from the surface of the sample has been assumed to vary slowly near the absorption edge and is neglected in the absorbance calculation.

For high pressure experiments with the DACs, bulk flakes with a size of ~ 100×100μm and thickness of ~ 10μm were prepared, and mounted into gasketed DACs. The pressure medium was a mixture of ethanol and methanol ~1:4. The applied pressure was calibrated by the standard method of monitoring the red shift of the ruby R1 photoluminescence line.

Photo-modulated reflectance (PR) spectrum was taken at ambient conditions. The feature shown corresponds to the critical point direct transition from the top of the valence bands to the conduction band edge. The fundamental bandgap energy was determined from the PR spectrum to be 1.57 eV, using the standard Aspenes fitting method [29]. This is in agreement with the gap energy defined by the crossing point of the steeply rising portion and the baseline of the micro-absorption curves, as well as the photoluminescence measurement. All optical experiments were carried out at room temperature (295 K).

Supplementary Note 6. AFM and Nano-Auger Electron Spectroscopy (AES) Measurements. The thicknesses of exfoliated layers were determined by AFM scanning using a Digital-Instrument atomic force microscope. To estimate the chemical composition of ReS_2 single crystals, Auger spectroscopy was performed using a field emission electron source and a multi-channel detector at ultra-high vacuum (low 10^{-10} mbar). A series of Auger spectra were measured on several different regions with an electron beam energy of 3 keV and a scan area of 50 μm × 50 μm. The S/Re stoichiometric ratio was estimated to be ~ 1.98 using the S 155 eV and Re 217 eV peaks and corresponding sensitivity factors, 4.7575 and 1.1260 [30].

Supplementary Note 7. High Resolution Transmission Electron Microscopy (HRTEM) study. To study the structure and define the stacking order of ReS_2, we deployed extensive high-resolution transmission electron microscopy (HRTEM) and electron diffractometry. In layered materials such as MoS_2 and ReS_2, the intensity of 00l electron diffraction spots carries information about the stacking order. For example, 2H stacking in MoS_2 will manifest itself as a strong 6.05 Å (0 0 2l) reflections, representing the interlayer stacking distance, and weaker (0 0 2l+1) reflections in between, resulting from the well-defined interlayer stacking. For clarity and comparison, we chose to describe the ReS_2 crystal by a 2T-ReS_2 (ICSD 81814) unit cell, which is a triclinically distorted 2H-MoS_2 structure consisting of two ReS_2 layers per unit cell. The distortions with respect to the MoS_2 cell are minor in the 001 and 100 directions, but are significant in the 010 axis, consistent with the Pearls distortion present in the structure. The electron diffraction patterns in Fig.2 (main manuscript) reveal that the ReS_2 crystal structure is similar to the structure files reported in the literature. Our TEM data show that these ReS_2 flakes are highly crystalline. Presence of high-intensity *h0l* and *0kl* diffraction peaks (from prismatic planes) indicates that the structure is not turbostratic in nature. After

orienting the crystal with the electron beam pointing at the [210] axis, the measured diffraction pattern consists of (1 $\bar{2}$ 0) and (0 0 2) reflections (main manuscript Figure 2). The lack of odd ((0 0 1), (0 0 3), (0 0 5), etc.) reflections suggests lack of specific (Bernal) stacking. After analysing the broadening in the (002l) reflections, we find that the interlayer spacing vary between 6.0 and 6.9 Å implying that the interlayer interaction is rather weak.

In summary, the TEM study confirms that the exfoliated ReS$_2$ flakes are highly crystalline, preserving perfect in-plane order. The structure shows no particular ordering in the stacking between layers and the degree of crystallinity is highly anisotropic. The distance between the individual layers varies by more than 15%, which is consistent with the very weak (18meV) interlayer binding energy. The week interlayer coupling, and the large variations in the interlayer distance suggest small in-plane displacements of the individual layers from their equilibrium positions, which is in turn consistent with the observed optical and electronic properties.

Supplementary References

23. A. Tanaka, N.J. Watkins, and Y. Gao, Hot-electron relaxation in the layered semiconductor 2H-MoS$_2$ studied by time-resolved two-photon photoemission spectroscopy, Phys. Rev. B 67, 113315 (2003)

24. C.H. Ho, Y.S. Huang, K.K. Tiong, and P.C. Liao, Absorption-edge anisotropy in ReS$_2$ and ReSe$_2$ layered semiconductors, Phys. Rev. B 58, 16130 (1998)

25. C. Muratore, V. Varshney, J.J. Gengler, J.J. Hu, J.E. Bultman, T.M. Smith, P.J. Shamberger, B. Qiu, X. Ruan, A.K. Roy, and A. A. Voevodin, Cross-plane thermal properties of transition metal dichalcogenides, Appl. Phys. Lett. 102, 081604 (2013)

26. S. Ghosh, W. Bao, D. L. Nika, S. Subrina, E. P. Pokatilov, C.N. Lau and A. A. Balandin, Dimensional crossover of thermal transport in few-layer graphene, Nature Mater. 9, 555-558 (2010).

27. A. A. Balandin, Thermal properties of graphene and nanostructured carbon materials, Nature Mater. 10, 569-581 (2011).

28. J. Wu, W. Walukiewicz, K. M. Yu, W. Shan, J. W. Ager, E. E. Haller, I. Miotkowski, A. K. Ramdas, & C. H. Su, Composition dependence of the hydrostatic pressure coefficients of the bandgap of ZnSe1-xTex alloys. Phys. Rev. B, 68, 033206 (2003)

29. D. E. Aspnes, Third-derivative modulation spectroscopy with low-field electroreflectance. Surf. Sci., 37, 418 (1973)

30. K. D. Childs, B. A. Carlson, L. A. Vanier, J. F. Moulder, D. F. Paul, W. F. Stickle, D. G. Watson, Handbook of Auger Electron Spectroscopy (eds. Hedberg, C. L.) (Physical Electronics, Eden Prairie, MN, 1995).